Available online at www.sciencedirect.com
SCIENCE DIRECT®
Journal of Nuclear Materials 336 (2005) 65–72
journal of nuclear materials
www.elsevier.com/locate/jnucmat

Pitting corrosion of the laser surface melted Alloy 600

Yun Soo Lim [a,*], Joung Soo Kim [a], Hyuk Sang Kwon [b]

[a] *Nuclear Materials Technology and Development Division, Korea Atomic Energy Research Institute, P.O. Box 105, Yusong, Taejon 305-600, South Korea*
[b] *Department of Materials Science and Engineering, Korea Advanced Institute of Science and Technology, 373-1, Kusung-Dong, Yusong, Taejon 305-701, South Korea*

Received 3 April 2004; accepted 26 August 2004

Abstract

The effect of laser surface melting (LSM) on the resistance to pitting corrosion of Ni-base Alloy 600 was investigated by a potentiodynamic polarization test in 1 M NaCl solutions at pH values of 4 and 10 at temperatures of 30, 60 and 90 °C. The pitting potentials of Alloy 600 were markedly increased by the LSM process, when compared with those of the non-laser treated Alloy 600. From the microscopic examination after the corrosion test, it was found that the pitting was initiated at the junction between a TiN inclusion and the matrix, possibly at the site of a sulfide physically associated with the TiN inclusion. The homogeneous micro-structure associated with the reduction of the inclusion size during the LSM process could be attributed to the improvement of the pitting corrosion properties in the LSM Alloy 600.

1. Introduction

Ni-base Alloy 600 (or Alloy 600), as the steam generator (SG) tubing material of nuclear power plants, has been reported to have suffered from various types of localized corrosion such as pitting, intergranular attack (IGA), intergranular stress corrosion cracking (IGSCC) and denting under pressurized water reactor operating conditions [1]. In particular, pitting corrosion is known to be caused by chloride-containing and/or oxidizing environments [2–4]. Under certain conditions, pitting can be associated with the development of stress corrosion cracking [5].

The inhomogeneities represented by non-metallic inclusions locally reduce the stability of the passive films, which consequently breakdown preferentially when exposed to aggressive environments, producing pitting corrosion. Recently Hur et al. [6,7] demonstrated that the pitting of Alloy 600 was initiated at the sites of sulfide inclusions physically associated with titanium nitrides. The role of a sulfide inclusion in stainless steels, as a site of pit initiation, has been well recognized over the past several decades [8–13]. A common observation is that the pit initiation occurs as a result of a micro-crevice formation at the inclusion/metal interface.

A laser surface melting (LSM) technique uses a laser beam as a heat source to modify the surface properties of materials, and it can be applied to improve the resistance to localized corrosion in alloys. From previous studies, it has been shown that the resistance to IGSCC of the sensitized Alloy 600 in sulfur-bearing environments [14] was

* Corresponding author. Tel.: +82 42 868 2341; fax: +82 42 868 8549/8346.
E-mail address: yslim@kaeri.re.kr (Y.S. Lim).

0022-3115/$ - see front matter © 2004 Elsevier B.V. All rights reserved.
doi:10.1016/j.jnucmat.2004.08.015

improved by LSM. Lim et al. [15] also revealed that LSM enhanced the resistance to IGA of the sensitized Alloy 600 in acid solutions, mainly due to the metallurgical changes induced by the laser treatment [16–18]. Stewart and Williams [12] conducted LSM on type 304L stainless steels, and in their work, LSM was shown to markedly improve the pitting resistance in neutral dilute chloride solutions. They found that LSM significantly reduced the size of the sulfide inclusions, and concluded that this was the most important effect of LSM leading to the improvement in the pitting resistance.

In the present work, the effect of LSM on the pitting corrosion properties of Alloy 600 was studied using a potentiodynamic polarization test in 1 M NaCl solutions at the pH values of 4 and 10 at several temperatures. The difference in the pitting corrosion resistance between the laser treated and non-laser treated alloys was compared and discussed by considering the micro-structure, the inclusions involved, and the corroded surfaces after the corrosion test.

2. Experimental procedures

2.1. Specimen preparation

Mill annealed Alloy 600 plates 1.6 mm thick were used in this study, and the alloy composition is listed in Table 1. The specimens were sealed in a quartz tube, solution annealed (SA) at 1050 °C for 30 min, and then water quenched (referred to as the SA Alloy 600).

Before the laser treatment, the SA Alloy 600 was polished with a 600-grit SiC paper to increase the absorption of the incident laser beam. A continuous CO_2 laser beam (maximum power of 4 kW) was used at a real laser power of 500 W and a scanning rate of 200 cm/min. The laser beam scan, blowing with a continuous flow of Ar (30 l/min.) to prevent oxidation of the melted region, was done with a beam diameter of 1 mm on the specimen surface and overlapped by half of the laser beam to get a large treatment area. The laser treated samples will be referred to as the LSM Alloy 600.

2.2. Potentiodynamic polarization test

Cu-wire was spot-welded to one side of each specimen, which was then mounted in epoxy resin, and ground to 2000 grade silicon carbide. To avoid crevice corrosion, the specimen–mount interface was carefully coated with a thin film of silicone sealant. Approximately 5×5 mm of the surface was exposed to the test solution. 1 M NaCl solutions at the pH values of 4 and 10 were chosen for the investigation. The pH values were adjusted using HCl and NaOH. The test solutions were deaerated with a nitrogen flow before and during each potentiodynamic polarization test.

The potentiodynamic polarization test was performed using a three-electrode cell system consisting of a saturated calomel electrode (SCE) as a reference, a platinum electrode as a counter, and a specimen as a working electrode. The sample was allowed to float to the corrosion potential for 2 h to attain a stable value before polarization. After obtaining the stable corrosion potential (E_{corr}), the potential was raised in the anodic direction, from −100 mV below E_{corr}, at a scan rate of 0.5 mV/s. All the potentials were quoted with respect to an SCE. The potentiodynamic polarization test was carried out at temperatures of 30, 60 and 90 °C, and repeated several times for each specimen to ensure reproducibility. The pit morphology subsequent to the potentiodynamic polarization test was examined with an optical microscope and a scanning electron microscope (SEM).

2.3. Micro-structural examination

For observation with an optical microscope and an SEM, the specimens were prepared by electrolytic etching with a solution of 2% HCl + 98% methanol at 6 V at room temperature. A transmission electron microscope (TEM, JEOL 2000FX II, operating voltage 200 kV) equipped with an energy dispersive X-ray spectroscopy (EDS) was also used to evaluate micro-structural changes resulting from the LSM process, and the TEM specimens were prepared by thinning them mechanically down to approximately 15 μm, followed by an electropolishing process.

3. Results

3.1. Potentiodynamic polarization test

Some of the potentiodynamic responses of the SA and LSM Alloy 600 in 1 M NaCl solutions are shown in Fig. 1(a) at pH 4 at 90 °C and Fig. 1(b) at pH 10 at 60 °C. By LSM, the E_{corr} of the SA Alloy 600 were

Table 1
Chemical composition of the specimen used (wt%)

Ni	Cr	Fe	C	N	S	Si	Mn	Al	Ti	Nb	Mg
Bal.	15.9	7.6	0.04	0.04	0.002	0.15	0.17	0.12	0.21	tr.	0.008

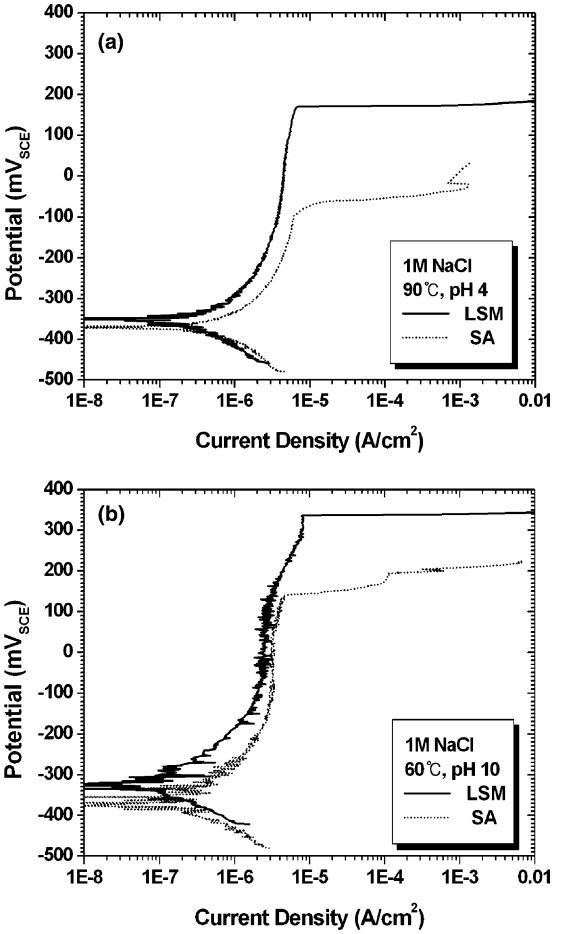

Fig. 1. Anodic polarization curves of the SA and LSM Alloy 600 in 1 M NaCl solutions (a) at pH 4 at 90 °C and (b) at pH 10 at 60 °C.

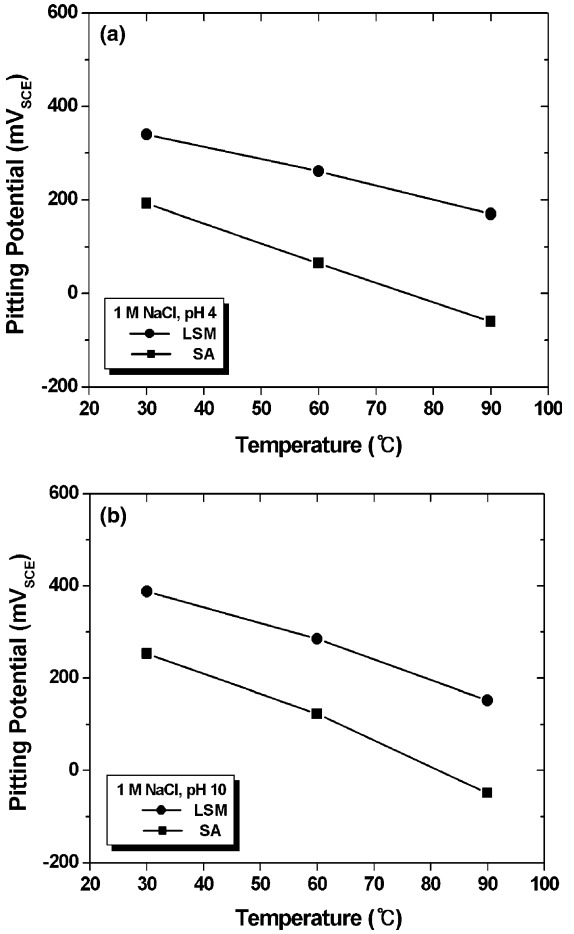

Fig. 2. Pitting potentials of the SA and LSM Alloy 600 in 1 M NaCl solution as a function of temperature at pH values of (a) 4 and (b) 10.

increased and the corrosion rates in the passive regime were reduced. However, their changes were not large. These results originated from the fact that the overall chemical composition of the LSM Alloy 600 was the same as that of the SA Alloy 600, since the laser beam was only used as a heat source. As a result, the general corrosion behaviors of Alloy 600 are hardly changed by the LSM process. This fact was also confirmed from a DL-EPR test in 0.01 M H_2SO_4 + 20 ppm KSCN solutions [15].

The increase of the pitting potential, as shown in the figures, was noticeable. Fig. 2(a) presents the pitting potential changes of both alloys depending on the temperature in the acid environments, and Fig. 2(b) in the alkaline environments. In any case, the pitting potential of Alloy 600 was increased by about 200 mV as a result of the LSM. From these results, it is evident that the LSM process markedly improved the pitting resistance of Alloy 600 in the chloride containing solutions. For a given alloy and temperature, the pitting potential in an acid environment is a little lower that that in an alkaline environment. Further, the pitting potentials of both alloys seemed to decrease in a linear manner within the range of the temperatures.

3.2. Micro-structural examination

Fig. 3 shows the typical micro-structure of the SA Alloy 600. By the solution annealing, all the intergranular and intragranular Cr-rich carbides were dissolved making a homogeneous micro-structure, except for the non-metallic inclusions randomly distributed over the specimen. The inclusions contained in the Alloy 600 were mostly identified as TiN and (Mg, Ca)S, and the sulfides were generally associated with the TiN, as was observed in previous studies [6,17,22].

Fig. 4 shows the cross-section of the micro-structure of the LSM Alloy 600. By the laser treatment, three

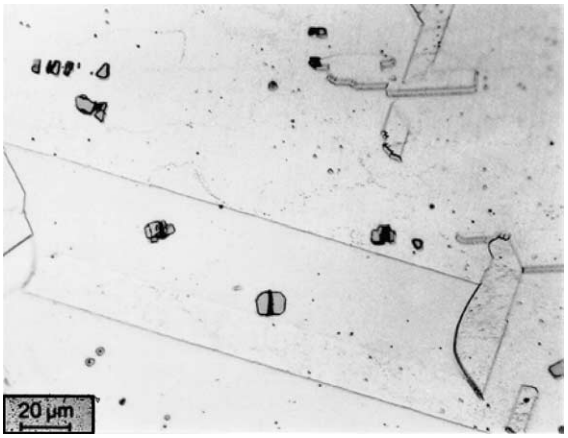

Fig. 3. Optical micrograph showing the micro-structure of the SA Alloy 600, etched in a 2% bromine + 98% methanol solution.

distinct zones were created: a laser melted zone (LMZ), heat affected zone (HAZ), and an unaffected bulk zone (matrix). The depth of the LMZ ranged from 150–200 μm, and the width of the HAZ was approximately 50 μm under the present LSM conditions. The micro-structural features of each zone of the Alloy 600 are well documented elsewhere [16], therefore, that of the LMZ, which is responsible for pitting corrosion, will be the focus of discussion in this paper.

The typical solidification morphology of the LMZ is cellular-dendritic, as shown in Fig. 5(a). Secondary and higher order dendritic arms were not significantly developed due to a high solidification rate. The primary arm

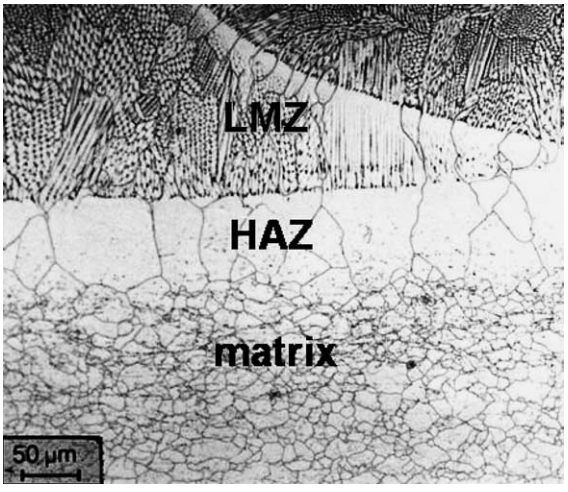

Fig. 4. Optical micrograph showing the micro-structure of the LSM Alloy 600, etched in a 2% bromine + 98% methanol solution.

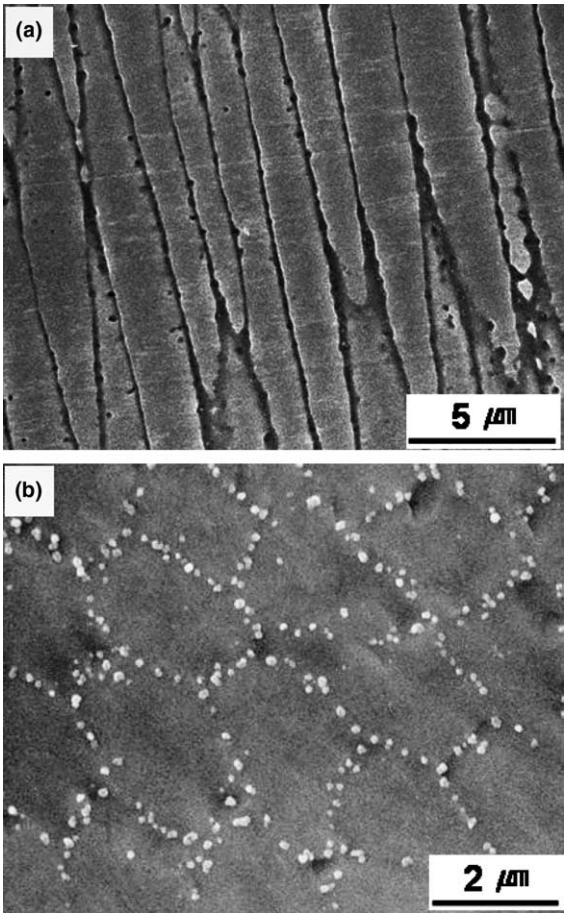

Fig. 5. SEM micrographs showing the (a) solidification morphology and (b) particle distribution in the laser melted zone of Alloy 600.

spacing was approximately 2 μm. Within each grain, all the cellular dendrites had the same shape, demonstrating that they grew in a specific crystallographic direction in a grain, i.e., ⟨1 0 0⟩ in the case of a cubic metal [19]. The pre-existing non-metallic inclusions in the SA Alloy 600 before LSM (Fig. 3) were not found in the LMZ. This result originated from the fact that they had been completely melted/dissolved due to the high energy density of the laser beam.

Fig. 5(b) shows the particles formed in the LMZ. From the TEM analysis, it was revealed that the intergranular and intragranular Cr-rich carbides were not precipitated during the LSM process [16]. The microstructure of the LSM specimen, therefore, can be compared with that of the SA specimen in the absence of the Cr-rich carbides. It is evident from Fig. 5(b) that tiny particles were formed by LSM, which were distributed along the cell boundaries and hardly found inside the cells. They were found all-over the LMZ and their distri-

bution exactly denoted the solidification morphology of the LMZ.

The tiny particles along the cell boundaries were identified as TiN and MgS type particles from various electron microscopy analyses, and the details are given elsewhere [16,17]. Fig. 6 shows some of the typical particle morphologies. The average sizes of the TiN and MgS particles were very small, approximately 100 nm or less in diameter. MgS was always found attached to TiN, suggesting that MgS had nucleated and grown on the TiN. The number density of the TiN was roughly estimated to be 10^{13} to 10^{14} particles/cm^3. On the other hand, the number of MgS particles observed was much lower than that of the TiN particles. Their formation can be attributed to the melting/dissolution of the pre-existing coarse TiN and MgS inclusions (Fig. 3) in the SA Alloy 600 and the subsequent re-precipitation as tiny particles during the LSM process [17]. The solid solubilities of N, Mg and S in Ni are known to be negligible [20]. Therefore, the elements preferentially segregated on the cell boundaries during solidification are expected to precipitate as TiN and MgS with a low free-energy formation, even though the original contents of N, Mg and S are i.e., only 400 ppm, 80 ppm and 20 ppm in the SA Alloy 600, respectively.

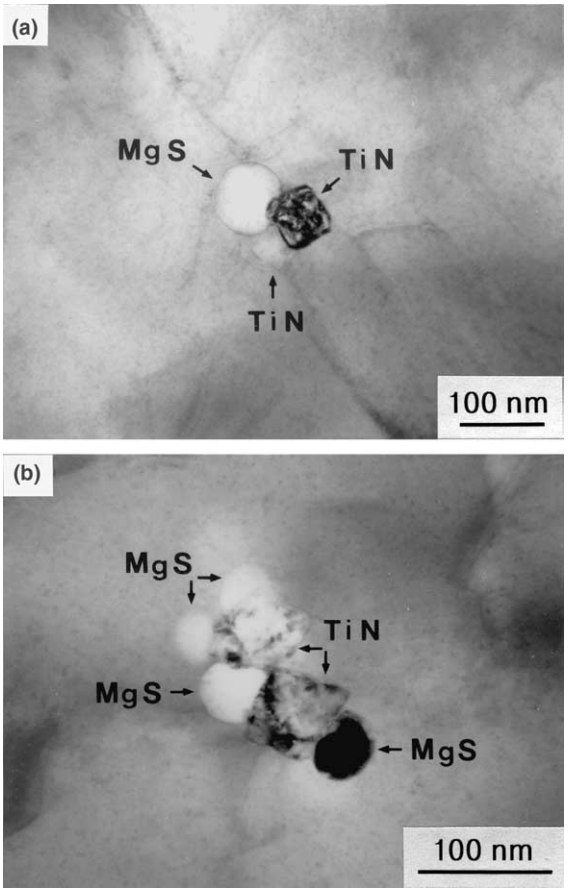

Fig. 6. Bright field images of the two types of particles (TiN and MgS) precipitated in the laser melted zone of Alloy 600.

3.3. Corroded surface morphology

Fig. 7 shows the early stage of a pit initiation in the SA Alloy 600 after the potentiodynamic polarization test. In this figure, the TiN inclusion itself did not dissolve, and a corrosive attack was initiated at the periphery of the TiN. The corrosion potential of the TiN coating layer was reported to be 400 mV higher than the mill-annealed Alloy 600 substrate in a 0.01 M NaCl solution [21]. Therefore, the TiN inclusion acts as a cathode and the matrix near the junction between the TiN and the Alloy 600 is preferentially corroded by the galvanic coupling effect, making a micro-crevice, even in the case of the absence of pit initiators such as sulfides in the chloride containing solutions.

Pit morphologies after a significant growth of the pits were quite different in both test specimens. Fig. 8(a) shows the typical pit appearance in the SA Alloy 600 under the present testing conditions. Irregularly shaped deep pits, with crystallographic facets, are found in the figure. Inside the pit, non-dissolved TiN inclusions are seen. By the laser treatment, a significant change in the pitting morphology took place. Round and shallow forms of attack were observed in the LSM Alloy 600, as shown in Fig. 8(b). The attacked morphology in the LSM Alloy 600 denoted exactly the solidification micro-structure, i.e., cellular-dendritic morphology. It results from the micro-segregation during solidification. Cr was more enriched along the cell boundaries due to the micro-segregation occurring during the LSM process

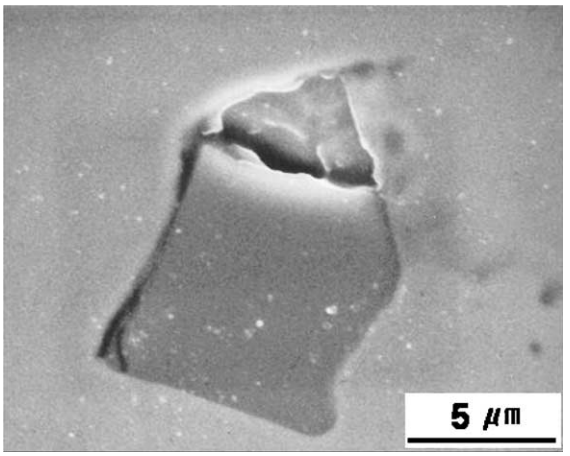

Fig. 7. SEM micrograph showing the early stage of a pit initiation at the periphery of a TiN inclusion in the SA Alloy 600.

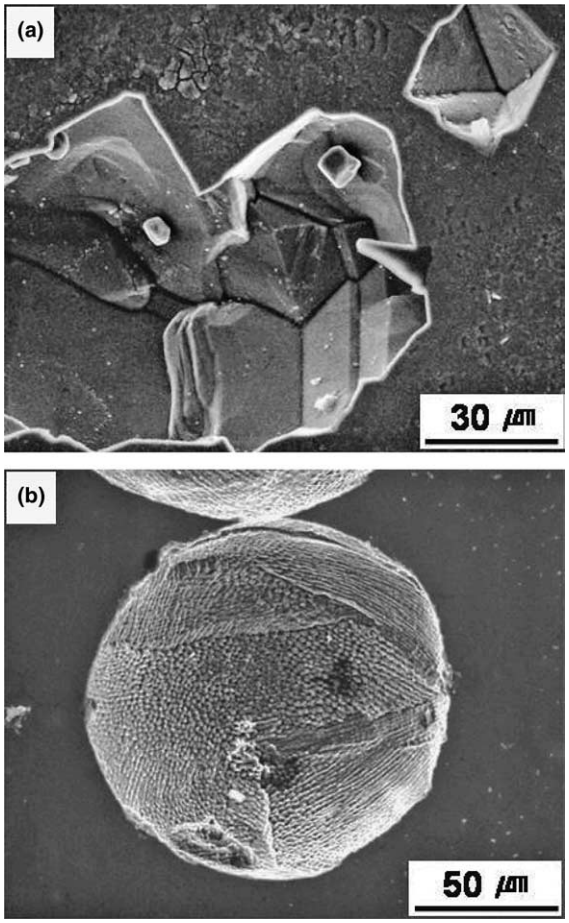

Fig. 8. Pit morphologies on the (a) SA Alloy 600 and (b) LSM Alloy 600 after potentiodynamic polarization test in a 1 M NaCl solution at pH 10 at 60 °C.

[16], therefore, the dissolution rate of the regions around the cell boundaries was different from that inside the cells due to the enriched Cr contents. Metal dissolution in accordance with the crystallographic planes, which is characteristic of the SA Alloy 600, did not occur in the LSM Alloy 600. Consequently, the major effect of the laser treatment on the pit morphology in the SA Alloy 600 would be the transition from a highly localized form of pitting of the SA Alloy 600 to a more generalized form of attack.

4. Discussion

From the results of the potentiodynamic polarization test, the beneficial effect of LSM in the resistance to the pitting corrosion of Alloy 600 was confirmed by a considerable increase of the pitting potentials in the chloride containing corrosive environments. The metallurgical changes induced by LSM could be responsible for the improvement in the pitting resistance of this alloy.

The nucleation sites of the pits are frequently found to be related to the inclusions on a metal surface. On stainless steels, for example, their location is usually found to be associated with the sulfide inclusions, as shown in the extensive works of Wraglen [8], Eklund [9], Castle and Ke [10], and Baker and Castle [11]. The presence of MnS inclusions in stainless steels increases the susceptibility of the steel to pit formation. Using SEM/EDS and Auger spectroscopy, Castle and Ke [10] and Baker and Castle [11] found that the pits were always initiated at the sites of Mn-enriched sulfides in type 316 SS, irrespective of whether or not the sulfides were isolated or combined with some oxides. In stainless steels, sulfide inclusions are commonly found to be associated with oxides or nitrides. In that case, pit initiation can be facilitated more since a deep micro-crevice is formed at the periphery along the inclusion/matrix interface due to the preferential dissolution of the sulfide.

On Alloy 600, however, the mechanism on where and how the pits nucleate is less well understood. An important observation made by several authors using SEM/EDS was a detection of strong sulfur peaks inside the propagating pits in spite of the very small amount of sulfur (0.001–0.008 wt%) in the bulk before the corrosion test [6,21]. The solid solubility of sulfur in Ni is known to be extremely low, therefore, sulfur ions as impurities in the bulk are present mostly as the sulfides of (calcium-substituted) MgS usually associated with titanium (carbo-) nitrides [6,22,23] or segregated in the grain boundaries [24]. In the present study with the SA Alloy 600, the corrosive attack was initiated at the TiN/matrix interface (Fig. 7). It is therefore suggested that, as in the case of stainless steels, pitting of Alloy 600 can be initiated at the sites of the sulfides attached to TiN in Alloy 600. Hur et al. [6] studied this very inception of pitting attack in Alloy 600. They also claimed that the dissolution of the sulfides attached to the TiN interface is the initial step in pit formation at these sites. Sulfide ions released by a corrosive attack on a sulfide inclusion spread out to the surrounding matrix surface [10], and accelerate (or activate) the anodic dissolution reaction [25,26]. Marcus et al. [26] investigated the influence of adsorbed sulfur on the electrochemical behaviors of Ni–25Fe alloy in acid solutions and, showed that the presence of the monolayer of the adsorbed sulfur enhances the dissolution rate and hinders the repassivation of the base metal.

A pitting potential is known to be that for nucleation of stable pit accompanied with film breakdown, or that for initiation of pitting corrosion rather than that for growth of pit [27]. Pit may grow at potentials between the pitting potential (E_{pit}) and the repassivation potential (E_{rp}). Once film is broken by chloride attack, anodic dissolution site occurs at the film broken, followed by

repassivation. At potentials noble to pitting potentials, repassivation occurs slowly so that the film broken site may develop into an occluded cell such as a pitting corrosion, which is characterized by the well known acidification and concentration of chloride ion. Thus, for the same alloy with different micro-structure, the pitting potential is determined by the resistance of the alloy to the chloride induced film breakdown and also to the formation of pit with a critical degree of occlusion at the film broken site, which is also influenced by the relative rates between anodic dissolution and repassivation. For the SA Alloy 600, coarse (Mg, Ca)S and angular TiN particles, shown in Fig. 3, acted as a preferential site for the film breakdown for pitting corrosion, and the micro-crevice formed at the angular TiN/matrix interface facilitated the formation of an occluded cell for pitting corrosion, as confirmed in Fig. 7. All of these contributed to reduce the pitting potential of the SA Alloy 600, irrespective of solution temperature and pH, as shown in Figs. 1 and 2. In contrast, the significant increase in pitting potential of the SA Alloy 600 by LSM, as presented in Figs. 1 and 2, is a result of the change in micro-structure in which coarse TiN and TiN/MgS inclusions (~10 μm) dissolved/melted, and then reprecipitated as tiny particles (~100 nm) forming very fine cell structure during LSM, as presented in Fig. 5. The fine LSM micro-structure with extremely small TiN/Mgs particles appears to be very difficult for the formation of an occluded cell on film broken site, which is confirmed by the shallow and hemisphere pit shown in Fig. 8(b).

The increase in the resistance to pitting corrosion by LSM was also reported in other alloy/environment systems [12,28]. Stewart and Williams [12] investigated the effect of LSM on the resistance to pitting corrosion of commercial purity (0.011 wt% S) and high sulfur (0.080 wt% S) type 304 stainless steels. They found that LSM refined the size and reduced the visible volume fraction of the sulfide inclusions in both alloys, resulting in the improvement of the pitting resistance by reducing the pit nucleation frequency in the passive regime. From their results, they concluded that a sulfide inclusion should have a certain critical size to initiate a propagating pit. If the size of a sulfide is below the critical size, the underlying surface can be easily repassivated. Searson and Latanision [13] also reached the same conclusion with AISI 303 stainless steels, in which small and rounded sulfide inclusions resulted in small non-propagating pits whilst a few large sulfides produced more damaging pits.

5. Conclusions

LSM had beneficial effects on the resistance to the pitting corrosion of Alloy 600 by markedly increasing the pitting potentials in the corrosive environments under investigation. Pitting was initiated at the junction between a TiN inclusion and the matrix, possibly at the site of a sulfide physically associated with the TiN inclusion in this alloy. Pit morphology after a significant growth of a pit was changed by LSM, from an irregularly shaped deep pit with crystallographic facets to a round and shallow form of attack.

The metallurgical changes induced by LSM were responsible for the improvement of the pitting corrosion properties of this alloy, and they can be summarized as follows. The first is that the solidified micro-structure caused by LSM was considerably homogeneous. Intergranular and intragranular Cr-rich carbides, which are harmful to the localized corrosion such as pitting and IGA/IGSCC by the creation of a Cr depleted zone, were not precipitated during the LSM process due to the fast cooling. Secondly, the pre-existing coarse TiN and sulfide inclusions in the SA Alloy 600, which act as the pit initiators for a stable pit growth, were completely melted/dissloved by the high energy of the laser beam. Lastly, the average sizes of the re-precipitated TiN and MgS during the LSM process were so small that they did not act as the initiation sites for the damaging pits.

Acknowledgments

This work has been carried out as a part of the Nuclear R&D Program by M.O.S.T. in Korea.

References

[1] T.U. Marston, R.L. Jones, in: Proceedings of the 5th International Symposium on Environmental Degradation of Materials in Nuclear Power Systems – Water Reactors, Monterey, California, 25–29 August 1991, American Nuclear Society, La Grange Park, Illinois, 1992.
[2] J. Hickling, N. Wieling, Corrosion 37 (1981) 147.
[3] J.R. Park, Z. Szklarska-Smialowska, Corrosion 41 (1985) 665.
[4] D. Choi, G.S. Was, Corrosion 46 (1990) 100.
[5] Z. Szklarska-Smialowska, Z. Xia, R.B. Rebak, P. Skulte, Corrosion 50 (1994) 279.
[6] D.H. Hur, K.M. Kim, J.S. Kim, Y.S. Park, J. Corros. Sci. Korea 27 (1998) 32.
[7] D.H. Hur, W.C. Kim, U.C. Lee, Y.S. Park, J. Corros. Sci. Korea 27 (1998) 43.
[8] G. Wranglen, Corros. Sci. 14 (1974) 331.
[9] G.S. Eklund, J. Electrochem. Soc. 121 (1974) 467.
[10] J.E. Castle, R. Ke, Corros. Sci. 30 (1990) 409.
[11] M.A. Baker, J.E. Castle, Corros. Sci. 34 (1993) 667.
[12] J. Stewart, D.E. Williams, Corros. Sci. 33 (1992) 457.
[13] P.C. Searson, R.M. Latanision, Corrosion 42 (1986) 161.
[14] J.H. Suh, J.K. Shin, S.-J.L. Kang, Y.S. Lim, I.H. Kuk, J.S. Kim, Mater. Sci. Eng. A 254 (1998) 67.
[15] Y.S. Lim, H.P. Kim, J.H. Han, J.S. Kim, H.S. Kwon, Corros. Sci. 43 (2001) 1321.

[16] Y.S. Lim, J.H. Suh, I.H. Kuk, J.S. Kim, Metall. Mater. Trans. A 28A (1997) 1223.
[17] Y.S. Lim, J.S. Kim, H.S. Kwon, Metall. Mater. Trans. A 32A (2001) 1248.
[18] Y.S. Lim, J.S. Kim, H.S. Kwon, Mater. Sci. Eng. A A279 (2000) 192.
[19] B. Chalmers, Trans. AIME 200 (1954) 519.
[20] T.B. Massalski, J.L. Murray, L.H. Bennett, H. Baker, L. Kacprzak (Eds.), Binary Phase Diagram, 1st Ed, 2, ASM, Metal Park, OH, 1986, p. 1529 (Mg–Ni), p. 1647 (N–Ni), p. 1751 (Ni–S).
[21] C.B. In, Y.I. Kim, W.W. Kim, J.S. Kim, S.S. Chun, W.J. Lee, J. Nucl. Mater. 224 (1995) 71.
[22] P.G. Caceres, B. Ralph, G.C. Allen, R.K. Wild, Philos. Mag. 59 (1989) 1119.
[23] P.G. Caceres, B. Ralph, G.C. Allen, R.K. Wild, Philos. Mag. 59 (1989) 1137.
[24] R.M Latanision, M. Kurkela, Corrosion 39 (1983) 174.
[25] J. Oudar, Br. Corros. J. 25 (1990) 21.
[26] P. Marcus, A. Teissier, J. Oudar, Corros. Sci. 24 (1984) 259.
[27] B.E. Wilde, in: B.F. Brown, J. Kruger, R.W. Staehle (Eds.), Localized Corrosion, NACE-3, Houston TX, 1974, p. 342.
[28] S.J. Lee, C.J. Park, Y.S. Lim, H.S. Kwon, J. Nucl. Mater. 321 (2003) 177.